Dalton Transactions

ROYAL SOCIETY OF CHEMISTRY

PAPER

View Article Online
View Journal | View Issue

Cite this: *Dalton Trans.*, 2024, **53**, 3132

Solvothermal synthesis of VO_2 nanoparticles with locally patched V_2O_5 surface layer and their morphology-dependent catalytic properties for the oxidation of alcohols†

Dorothea Gömpel,[a] Muhammad Nawaz Tahir, *[b,c] Mujeeb Khan, [d] Syed Farooq Adil, [d] Mohammed Rafi Shaik, [d] Mufsir Kuniyil, [d] Abdulrahman Al-Warthan[d] and Wolfgang Tremel *[a]

Received 10th August 2023,
Accepted 5th January 2024

DOI: 10.1039/d3dt02605a

rsc.li/dalton

Vanadium oxides are promising oxidation catalysts because of their rich redox chemistry. We report the synthesis of VO_2 nanocrystals with VO_2(B) crystal structure. By varying the mixing ratio of the components of a binary ethanol/water mixture, different VO_2 nanocrystal morphologies (nanorods, -urchins, and -sheets) could be made selectively in pure form. Polydisperse VO_2(B) nanorods with lengths between 150 nm and a few micrometers were formed at large water : ethanol ratios between 4 : 1 and 3 : 2. At a water : ethanol ratio of 1 : 9 VO_2 nanosheets with diameters of ~50–70 nm were formed, which aggregated to nano-urchins with diameters of ~200 nm in pure ethanol. The catalytic activity of VO_2 nanocrystals for the oxidation of alcohols was studied as a function of nanocrystal morphology. VO_2 nanocrystals with all morphologies were catalytically active. The activity for the oxidation of benzyl alcohol to benzaldehyde was about 30% higher than that for the oxidation of furfuryl alcohol to furfural. This is due to the substrate structure. The oxidation activity of VO_2 nanostructures decreases in the order of nanourchins > nanosheets > nanorods.

Introduction

Multivalent transition metal oxides (TMOs) display a wide range of intriguing and useful properties.[1–4] The ground state in TMOs is dictated by the valence state of the transition metal cations. In particular, the interplay between spin, orbital, charge, and lattice degrees of freedom has been studied in this category of solids with partially filled d-band.[5,6] Vanadium oxides are prototypical examples of multivalent TMOs with strongly correlated electrons.[7,8] They can undergo reversible metal–insulator phase transitions accompanied by changes in their crystallographic, magnetic, optical, and electrical properties.[7–10] Electron–lattice interactions and electron–electron correlation modify the properties of vanadium oxides for a variety of applications as chemical sensors,[11] electrode materials for lithium batteries,[12–14] capacitors and supercapacitors,[15] for electronic and optical[2] devices, and in particular in heterogeneous catalysis.[5,16–18] They are used for the production of important chemicals (*e.g.*, sulfuric acid, phthalic anhydride) and in the alleviation of environmental pollution (*e.g.*, nitrogen oxides from power plant flue gas).[19–21]

The high catalytic activity of V-oxides can be attributed to the ability of vanadium to easily switch between its V^{3+}, V^{4+} and V^{5+} oxidation states under the respective reaction conditions[22] and to the presence of unsaturated surface coordination sites, which represent oxygen-deficient defects that allow reactions involving bulk oxygen atoms.[9,23–26] Oxide surfaces undergo restructuring and can exchange oxygen atoms with the environment in ways that are difficult to predict.[27,28] VO_2 in particular is a catalyst for the desulfurization of dibenzothiophene,[29] the oxidative dehydrogenation of propane[30] or the electrochemical reduction of trinitrotoluene.[31]

Nanocrystals can serve as model catalysts with defined surface structure to study the structure–property relationships of powder catalysts. Apart from the oxidation state and crystallinity of vanadium oxide catalysts there are a variety of variables such as structure, surface area, morphology, surface

[a]*Chemistry Department, Johannes Gutenberg-Universität Mainz, Duesbergweg 10-14, D-55128 Mainz, Germany. E-mail: tremel@uni-mainz.de*
[b]*Interdisciplinary Research Center for Hydrogen Technologies and Carbon Management (IRC-HTCM), King Fahd University of Petroleum & Minerals KFUPM, Dahran 31261, Saudi Arabia. E-mail: muhammad.tahir@kfupm.edu.sa*
[c]*Interdisciplinary Research Center for Hydrogen and Energy Storage (IRC-HES), King Fahd University of Petroleum and & Minerals, Dahran 31261, Saudi Arabia*
[d]*Department of Chemistry, College of Science, King Saud University, P.O. Box 2455 Riyadh 11451, Kingdom of Saudi Arabia*
† Electronic supplementary information (ESI) available. See DOI: https://doi.org/10.1039/d3dt02605a

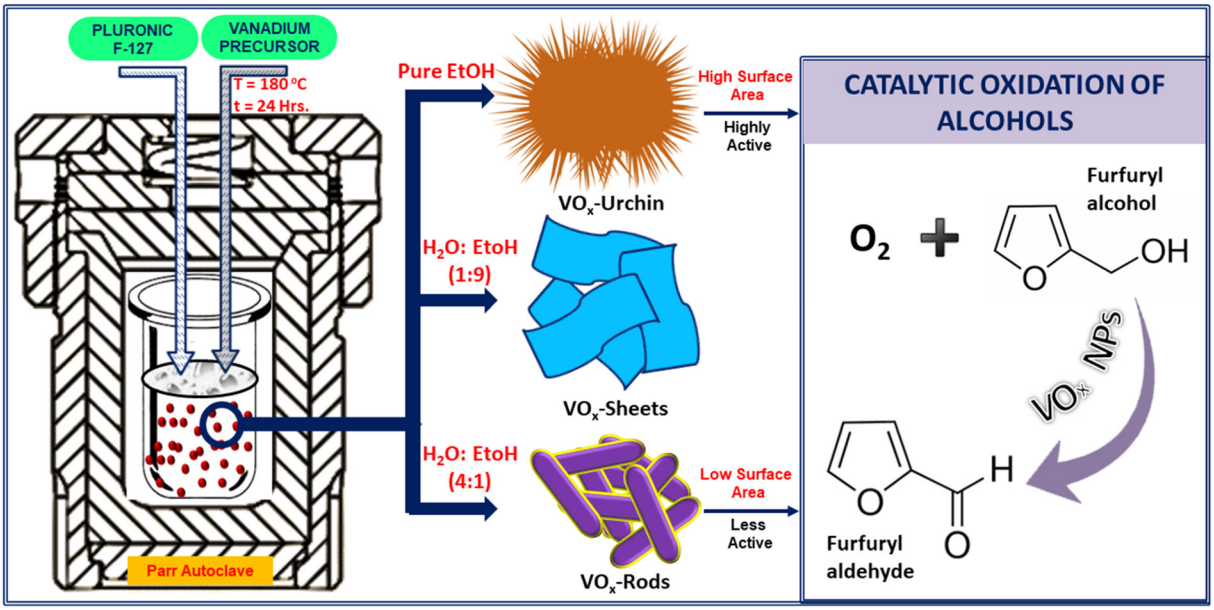

Scheme 1 Preparation of VO_2 nanoparticles with different morphologies and their catalytic applications in the oxidation of furfuryl alcohol.

wetting and interface interactions.[32] Colloidal synthesis allows the controlled preparation of metal oxide nanocrystals with defined and uniform morphology. Different facets of a nanocrystal have different surface energies, surface structures, and chemical reactivity, which can significantly determine catalytic performance. By controlling the morphology and size of the nanocrystals, it is possible to tune the exposed facets and enhance the catalytic activity and selectivity for a given reaction.[22,33,34]

The activities of nanostructured VO_x catalysts have been reported as a function of crystal morphology, crystal size and surface area.[35,36] Most of these studies, however, have been carried out with Magneli-type vanadium oxides such as V_nO_{2n+1} (V_3O_7, V_4O_9, and V_6O_{13}),[9] whereas morphology-dependent catalytic properties of VO_2 NPs have rarely been reported.[29] Several routes have been reported for the synthesis of VO_2 and other vanadium oxide nanocrystals.[37–40] The most common ones are based on hydro- or solvothermal techniques.[41] The choice of the solvent controls the reactivity, solubility and the diffusion of the precursors.[42] In binary solvent mixtures these factors can be tuned accurately and independently. This allows the preparation of nanocrystals with different morphologies, *e.g.*, spheres,[43–45] rods,[46–49] sheets,[50–53] and urchins[54,55] only by varying the volume ratio of the solvents.[56]

Sheet- and urchin-like morphologies are the most promising options for large surface areas, but the morphological effects can be offset by the particle size. Often the crystallites are several hundred nanometers in diameter. This leads in total to a significant reduction of the surface area. Therefore, a synthesis of nanometer-sized urchins and sheets is highly desirable. This requires the reactivity during the reaction to be fine-tuned to prevent uncontrolled aggregation into larger particles.

Here we describe the solvo-/hydrothermal synthesis of VO_2(B) nanorods and VO_2 nanosheets and -urchins. Therefore, the effect of solvent, especially the impact of chain length of aliphatic alcohols and the composition of binary mixtures on morphology and phase of VO_2 nanoparticles was explored systematically. The catalytic activity of VO_2 nanoparticles with different morphology and active surface area was tested for the oxidation of benzyl alcohol to benzaldehyde and furfuryl alcohol to furfural as a model reaction (Scheme 1). To the best of our knowledge, this is the first investigation of the catalytic properties of VO_2 nanoparticles in oxidation reactions as a function of particle size and morphology.

Results and discussion

The morphology of the nanoparticles was controlled by the reaction conditions, *i.e.*, by the solvent composition in the solvothermal reaction.[57,58] For this purpose, the synthesis of vanadium oxide nanoparticles was carried out in water/ethanol mixtures with different mixing ratios. The other reaction variables (reaction time, temperature, amount of pluronic capping agent and the concentration of the output compound) were kept constant.

The electron micrographs in Fig. 1 show that the morphology of the VO_2 nanoparticles is determined by the composition of the solvent mixture. The ratio of water to ethanol was systematically varied between 0% (pure water) and 100% (pure ethanol). Nanorods with very different aspect ratios formed in water (Fig. 1a). The length of the rods varied between 150 nm and several micrometers, while the width was between 20 and 200 nm. At water to ethanol ratios of 4 : 1 (20 mL : 5 mL, Fig. 1b) and 3 : 2 (15 : 10 mL, Fig. 1c), the morphology was

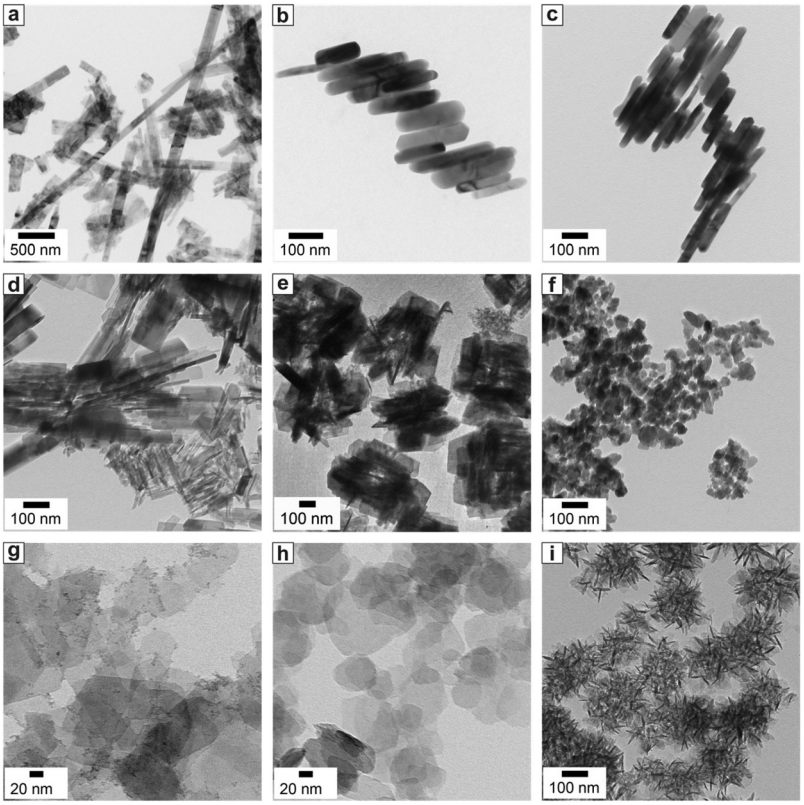

Fig. 1 TEM micrographs of the reaction products with different water : ethanol ratios. (a) pure water (25 mL : 0 mL), (b) 4 : 1 (20 mL : 5 mL), (c) 3 : 2 (15 mL : 10 mL), (d) 2 : 3 (10 mL : 15 mL), (e) 1 : 4 (5 mL : 20 mL), (f) 1 : 9 (2.5 mL : 22.5 mL), (g) 1 : 49 (0.5 mL : 24.5 mL), (h) 1 : 82.3 (0.3 mL : 24.7 mL) and (i) pure ethanol (0 mL:25 mL).

similar (nanorods), but the rods were significantly smaller and less polydisperse than when synthesized in pure water. Their width was in the range between 20 and 80 nm and their length between 100 and 220 nm. There was no visible difference in the morphology of the nanorods from water : ethanol mixtures between water : ethanol ratios of 4 : 1 and 3 : 2. The particles remained rod-like for higher ethanol concentrations. However, their polydispersity increased again (Fig. 1d, water : ethanol ratio 2 : 3). At a water : ethanol ratio of 1 : 4, the rods agglomerated into disordered bundles (Fig. 1e), and at a ratio of 1 : 9, nanorods no longer formed. The particles became increasingly isotropic but without defined morphology (Fig. 1f).

At high ethanol concentrations (water : ethanol < 1 : 49), a significant change in morphology occurred, and sheet-like nanocrystals with a narrow size distribution were formed (Fig. 1g and h).

The morphology of some nanoparticles in Fig. 1g is reminiscent of structures obtained at a water–ethanol ratio of 1 : 9 (Fig. 1f). In both cases, the diameter of the sheets was about 50–70 nm. The thickness of about 5 nm can be deduced from some sheets that were oriented vertically on the grid accidentally. Nanoparticles synthesized in pure ethanol have urchin-like morphologies with a total diameter of about 200 nm (Fig. 1i), as illustrated in Fig. 2. The wet chemistry methods used for the synthesis of nanoparticles are ideal to control

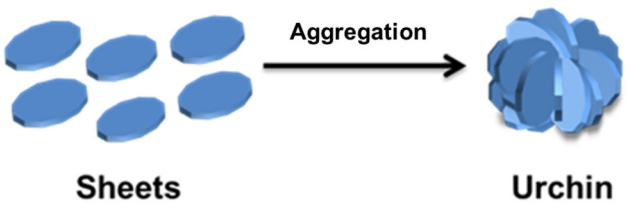

Fig. 2 Schematic representation of the morphological relation between the sheets and urchins.

the morphology, size and composition. In particular, hydrothermal/solvothermal methods[59,60] where the solubility and re-precipitation of the precursors define the number of nuclei and the growth (size) of particles, can be utilized to control size and morphology. We used pure water (high dielectric constant) as solvent, resulting in a medium of low supersaturation, leading to a small number of nuclei and the formation of larger particles (nanorods). However, a gradual increase of the amount of ethanol (low dielectric constant that provides a medium with high supersaturation), the number of nuclei increases and ultimately results in small size particles sizes. Using pure ethanol, where the number of nuclei is highest, these nuclei combine to form nano-urchins to compensate

their surface energy. Basically, a single urchin consists of several sheets that agglomerate in a random manner. Therefore, the crystallinity of the resulting particles is very low as indicated by the very broad diffraction intensities (Fig. 3, *vide infra*). The driving force for this agglomeration could be the different colloidal stability of the sheets depending on the solvent. Moreover, the sheets that compose the nano-urchins were smaller than free-standing sheets, thereby favoring aggregation. Thus, the composition of the solvent mixture is an effective means of controlling the morphology of vanadium oxide nanoparticles. By varying the water : ethanol ratio, three different morphologies – rods, sheets, and urchins (resulting from sheet agglomeration) – could be made in a reproducible fashion. We note that the surfactant F-127 helps to obtain well dispersed (but not porous) nanoparticles as indicated by the TEM images in Fig. S1.† The morphology of the nanoparticles was primarily controlled by using different ethanol : water ratios.

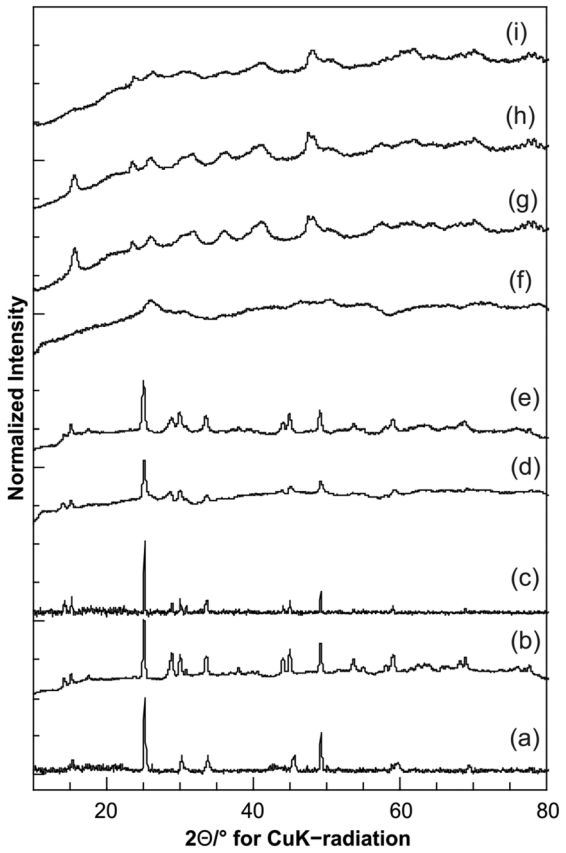

Fig. 3 Powder X-ray diffraction patterns of the reaction products prepared with different water : ethanol ratios. (a) Pure water (25 mL : 0 mL, VO_2 nanorods), (b) 4 : 1 (20 mL : 5 mL, nanorods, less polydisperse), (c) 3 : 2 (15 mL : 10 mL, nanorods, less polydisperse), (d) 2 : 3 (10 mL : 15 mL, nanorods, more polydisperse), (e) 1 : 4 (5 mL : 20 mL, nanorods agglomerated into disordered bundles), (f) 1 : 9 (2.5 mL : 22.5 mL, isotropic nanoparticles, no distinct morphology), (g) 1 : 49 (0.5 mL : 24.5 mL, sheet-like nanoparticles with narrow size distribution), (h) 1 : 82.3 (0.3 mL : 24.7 mL) and (i) pure ethanol (0 mL : 25 mL, sheets agglomerating to urchin-like morphologies).

Fig. 3 shows the PXRD patterns of the products prepared at different water : ethanol ratios. The diffractograms of the products prepared with water and water : ethanol ratios between 5 : 1 and 1 : 4 show the reflections of VO_2(B) (JCPDS 812392, Fig. 3a–e). Some reflections display sharper profiles than others. This is indicative of strongly anisotropic crystallites, as the crystallite size is inversely proportional to the full width at half maximum (fwhm).[61,62] Anisotropic crystallite sizes are in good agreement with the rod-like morphology of the nanoparticles (Fig. 3a–e), where the reflections should be sharper along the lattice direction associated with the long axis of the rods. For the rods obtained in pure water, the 00*l* reflections are weak. For the product obtained at a water : ethanol ratio of 1 : 9 (Fig. 3f), there or virtually no resolved reflections *i.e.*, the intensities of the X-ray diffraction patterns are extremely broad (compared to the diffractograms in Fig. 3a–e). The principal reflection is roughly at the same 2θ value as that for VO_2(B), indicating that the main product is also VO_2(B), albeit with very low crystallinity, *i.e.*, no long range order.

The PXRD patterns of the sheet-like products prepared with an ethanol excess (water–ethanol ratio < 1 : 49, Fig. 3g–i) also show broad reflections, indicating a low crystallinity. However, the weak reflection at $2\theta = 15.7°$ in Fig. 3g and h, which is not present in the sample prepared from pure ethanol, does not match the diffraction pattern of VO_2(B). Its position roughly corresponds to the stacking separation of layers in the structure of layered vanadium oxides (like V_2O_5), although no other reflections of V_2O_5 are present. This might be compatible with the formation of a second phase which may be present as a surface (mono)layer on the crystallites of VO_2(B), but might also be due to the sheet-like structure. The remaining broad intensities match in essence the diffraction pattern of VO_2(B), indicating that it is still the principal phase, although the reflections are also very broad and weak. The diffractogram in Fig. 3i is again not well defined, and the broad reflections are in harmony with the morphology of the particles seen in the TEM images (Fig. 3g–i). These products are made up of nanostructures with thin layers forming sheets or urchins. Typical for layered structures (stacked in a random manner) are broad reflections with partial overlap. The overall crystallinity of the samples is very low, resulting in weak scattering (and broad/weak reflections). Due to the poor crystallinity and the lamellar morphology it was difficult to clearly assign individual reflections and to assign the crystalline phase unambiguously. The change in morphology from rod- to sheet-like structures observed in the TEM would be compatible with a change in crystal structure of VO_2(B) to a sheet-like structure and possibly the formation of a surface layer containing fragments of the V_2O_5 structure. This assumption would also be in harmony with a Raman band at ~990 cm^{-1} (Fig. 5, *vide infra*) that indicates the presence of polymeric V_2O_5[63,64] containing distorted VO_5 pyramids sharing edges and corners as structural motif, while VO_2 (whose structure is based on edge-sharing VO_6 octahedra) is responsible for the remaining bands.[65]

This might arise from a "monolayer" of V_2O_5 on the surface of the VO_2 nanocrystals (that does not show up in the X-ray

diffractograms due to the absence of long-range order). Although the XPS spectra (Fig. 7, *vide infra*) could indicate that vanadium remains in oxidation state +4 (V 2p at 516.9 eV) consistent with a VO_2 composition the V 2p signals of V^{4+} and V^{5+} are to close (516.3, 517.3 eV)[66] to allow for a clear distinction.

The VO_2 nanorods, -sheets and -urchins were characterized by Raman spectroscopy (Fig. 5). The Raman spectrum of the nanorods shows bands at 283 and 406 cm^{-1} that can be assigned to V–O bending vibrations. The band at 477 cm^{-1} belongs to the V–O–V bending vibration, and the broad peak at 526 cm^{-1} corresponds to the stretching mode of triply coordinated V_3–O. The V_2–O band is located at 695 cm^{-1} whereas the V–O stretch appears at 878 cm^{-1}. Additionally, there is another band at 929 cm^{-1} which is attributed to a (local, *i.e.*, defect-related) V^{4+}=O moiety.[67]

The strong Raman peak at 995 cm^{-1} might be caused by the V–O stretching mode of a V_2O_5 surface layer.[63,64,68,69] Still, the Raman and X-ray data corroborate that the principle phase of the rods is VO_2. The different signal-to-noise ratios between sheets and urchins on one hand and rods on the other hand are due to different filters. The nanosheets and -urchins decompose under the measurement conditions for the rods. Therefore, the radiation intensity is lower for the sheets and urchins, while no peaks were observed for the rods. Since the local structure of the phases crystallizing in sheet and urchin form is not complete from the PXRD and the vibrational spectra, it remains difficult to assign the bands and phase identity unambiguously. Both, urchins and sheets, exhibit their strongest band at the same wavenumber (855 cm^{-1}). This position is typical of a V–O stretch. Additionally, a weak band appears at 366 cm^{-1}, which is due to V–O bending modes.[70] The Raman spectra suggest in agreement with the PXRD and IR data that the sheets and urchins have the same structure, because they show the same characteristic bands. The difference in fwhm of the VO_2 urchins and sheets is due to their respective morphology. The urchins show a higher degree of disorder as the petals are randomly oriented which in turn leads to a strong peak broadening in the Raman spectrum.

To further characterize the nanosheets, their composition was examined by energy dispersive X-ray spectroscopy (EDX, Fig. 6a). EDX confirms the presence of vanadium, oxygen, carbon and copper in the sample. The copper signal is from the copper grid on which the sample was measured. In addition, the carbon signal is likely caused in part by (i) the carbon coating on the grid. The carbon signal further originates (ii) from the organic components that serve as capping agents for the nanoparticles. The FT-IR spectrum of the sheets shows the presence of alkyl groups (Fig. 4). Therefore, the layers are composed of vanadium and oxygen, while part of the carbon signal likely originates from the ligands covering the nanoparticles. Fig. 6b shows a dark field image of the nanosheets with a size between 50 and 70 nm. Here, upright sheets with a thickness of 5 nm can be seen. Some electron diffraction patterns of the sheets are shown in Fig. 6c and d. Fig. 6c shows the patterns within the sheet layer. The sheet spacings are 6.6 Å and 23.8 Å (compatible with the VO_2(B)

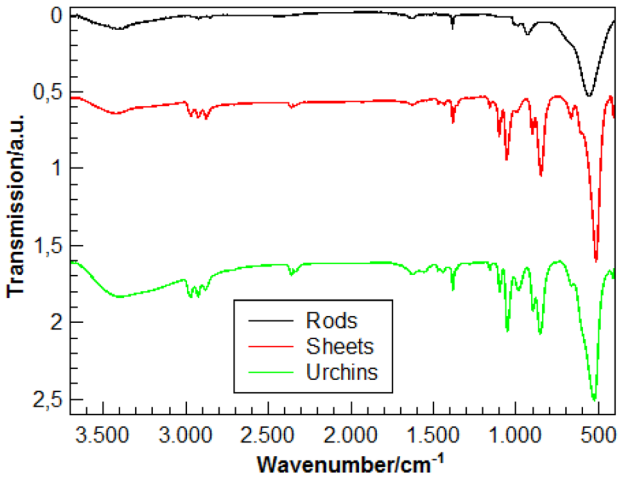

Fig. 4 IR spectra of the VO_2 nanorods (black), VO_x nanosheets (red) and VO_x nano-urchins.

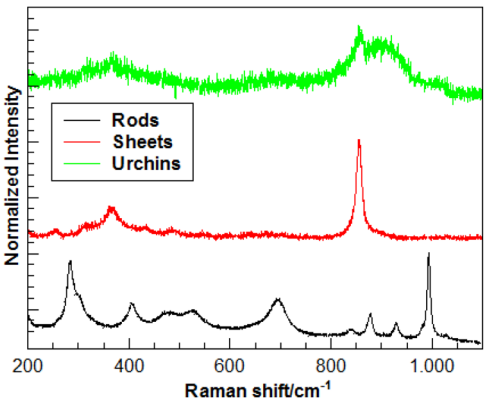

Fig. 5 Normalized Raman spectra of the VO_2 nanorods (black), nanosheets (red) and nano-urchins (green).

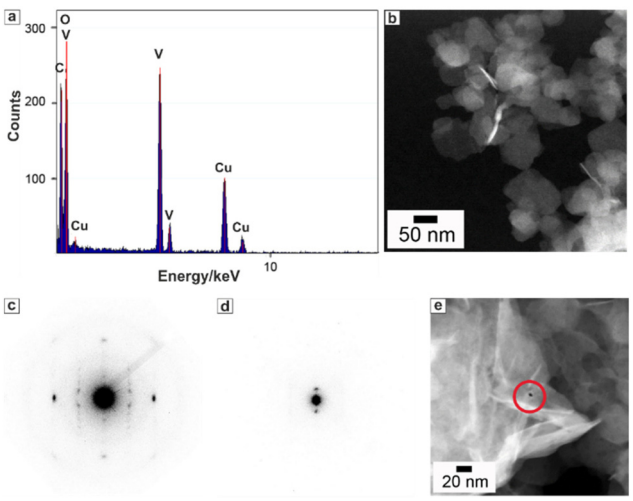

Fig. 6 (a) TEM EDX, (b) darkfield image, (c and d) electron diffraction patterns and (e) darkfield image showing radiation damage of the VO_2 sheets.

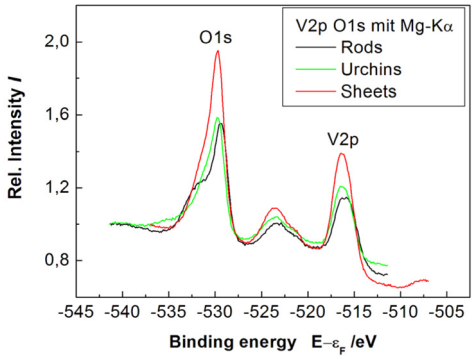

Fig. 7 XPS data of VO_2 nanorods (black), VO_2 nanosheets (red) and -urchins (green).

structure[10]) with systematic extinctions along the short axis. A diffraction pattern from the side of a platelet is shown in Fig. 6d, which shows spacings of 14.7 Å. Overall, the reflections are very broad, and the crystallinity of the associated phase is very low. Therefore, it was not possible to determine the cell parameters of the VO_2 sheets by electron diffraction, especially since the material is radiation sensitive. The sheets (with the organic surface ligands) decompose under the beam. Either bubble formation or hole etching occurs as in Fig. 6e (red circle), which prevents a structure determination by automated diffraction tomography (ADT).[71–73]

Finally, the oxidation state of the vanadium atoms in the vanadium oxide nanoparticles was determined by XPS spectroscopy. In the XPS spectra (Fig. 7), the oxidation state of the respective atoms determines the peak position *via* the electron binding energies (or electron work functions). The nanorods, -urchins, and -sheets show the vanadium 2p peaks at 516.4 eV. The assignment of oxidation states (V^{4+} *vs.* V^{5+}) based on XPS data is not unambiguous, because the V 2p signals of the different oxides may appear at similar energies (516.3, 517.3 eV) and the value for the nanorods, -urchins, and -sheets (516.4 eV) is in between. Moreover, the oxygen 1s peak (530 eV) which could not be deconvoluted agrees for the three particle types, *i.e.*, nanorods, -urchins, and -sheets contain vanadium in the same oxidation states. Since the phase identity of the *crystalline* fraction of the nanorods is assured from the PXRD diffractograms and the Raman spectra, (Fig. 3 and 5) the urchins and -sheets also contain V^{4+}, *i.e.*, VO_2. The positions of the vanadium 2p (516.9 eV) and oxygen 1s orbitals (530 eV) agree with literature data for the respective bands.[74,75]

Catalytic evaluation

Many partial oxidation catalysts in industrial applications are based on vanadium and molybdenum oxides.[5,19–21,32] The partial oxidation of alcohols is particularly well studied because the resulting aldehydes and ketones are important and reactive intermediates in industrial chemistry. Highly active catalysts have been developed and optimized mostly empirically by high-throughput methods. The structure of these catalysts often consists of several cooperating phases. Moreover, the structure of the surface, where the catalytic reaction proceeds, is rich in structural defects and structurally different from the bulk. Therefore, nanoparticles with a large variety of possible active surface sites are interesting targets for experimentation. They are also difficult to prepare in pure form by high-throughput reactions. In this context, VO_2 nanoparticles with different morphologies are interesting model systems.

Here we investigate the effect of particle morphology on the catalytic performance of the VO_2 nanoparticles. All three morphologies, *i.e.*, VO_2 nanorods, -sheets, and -urchins were used as catalysts for the oxidation of two model compounds, benzyl alcohol and furfuryl alcohol. The experimental procedure for the oxidation of alcohols and GC chromatogram showing product purity of furfuryl alcohol and benzyl alcohol oxidation using VO_2 nano-urchins is shown in the ESI Fig. S2 and S3.† Oxidation reactions were performed under identical conditions reaction temperature 150 °C with O_2 gas as oxygen source for comparison. All three VO_2 particle morphologies were active for the oxidation of benzyl alcohol to benzyl aldehyde. The results in Table 1 show that the catalytic efficiency is morphology dependent. VO_2 nano-urchins showed highest yield (~100%) and a specific activity of 3.01 mmol g^{-1} h^{-1}. VO_2 nanorods showed the lowest yield of ~71% with a specific activity of 2.13 mmol g^{-1} h^{-1}. VO_2 nanosheets yielded a slightly lower conversion (87%) than urchins. For the oxidation of furfuryl alcohol to furfural the catalytic activity was significantly lower (Table 2) with a maximum conversion of ~67% for the urchin morphology. Still, the trend in terms of morphology dependence remained. VO_2 urchins showed the highest conversion (67%), VO_2 nanosheets a slightly lower conversion of ~60%. while the lowest conversion (~33%) was achieved with VO_2 nanorods. The lower product conversion during the oxidation of furfuryl alcohol compared to that of benzyl alcohol can may be attributed to the O heteroatom in the furfuryl ring system.

Surface area analysis (using multipoint BET measurement) shows the correlation between the catalytic activity of the VO_2 nanocatalysts and their surface area. VO_2 nanorods have a surface area of 21.7 m^2 g^{-1} measured, which is within the typical size range for nanorods.[76] The surface area of the urchins and sheets is significantly higher (124.6 and 73.9 m^2 g^{-1}, respectively) due to their higher surface-to-volume ratio. Specifically, the surface area of the VO_2 urchins is remarkably

Table 1 Morphology-dependent catalytic performance of VO_2 NPs for the conversion of benzyl alcohol to benzaldehyde

Morphology (VO_2 NPs)	Benzyl alcohol → Benzaldehyde Conversion (%)
Nano-urchins	100
Nanosheets	87
Nanorods	71

Table 2 Morphology-dependent catalytic performance of VO_2 NPs for the conversion of furfuryl alcohol to furfural

Morphology (VO_2 NPs)	Furfuryl alcohol → Furfural Conversion (%)
Nanourchins	67
Nanosheets	60
Nanorods	33

high compared to the reported surface areas of sheet- and urchin-like particles. Xu *et al.*[77] synthesized urchin-like V_2O_3 particles with a surface area of 48.57 $m^2\ g^{-1}$, while Pan *et al.*[78] obtained flower-like V_2O_5 with a surface area of 33.64 $m^2\ g^{-1}$. The differences in surface area are due to the difference in the overall size of the particles, which was in the nanometer range for the VO_2 urchin-type particles, while the diameters of the particles reported in the literature are in the micrometer range. Another factor is the thickness of the "petals". The thinner the petals, the larger the surface area. Pang *et al.*[79] obtained flower-like V_4O_9 microparticles with a specific surface area of 107.9 $m^2\ g^{-1}$, which can be attributed to the thin layers of 2 nm. The surface areas of nanoparticles are usually much larger than those of bulk vanadium oxides (*e.g.*, V_2O_5 with 8.4 $m^2\ g^{-1}$). When correlating the surface areas with the catalytic performance, the catalytic performance is high with increasing surface area. The highest conversion of alcohol to aldehyde is obtained for urchins and sheets, while the lower active surface area of nanorods entails a lower conversion. For all morphologies there are indications for surface layers with local V_2O_5-type characteristics (without long-range order). Since these surface layers with local V_2O_5-type moieties but without translational symmetry are present on all surfaces, they affect the catalytic activity of the VO_2 particles in a comparable way. To confirm that enhanced catalytic activity is related to VO_2 nanomaterials with traces of V_2O_5 surface patches (VO_2/V_2O_5 hybrid) and not just due to the surface V_2O_5 layer, we provide a comparison based on previous reports.[81–86] (Table S1†). The results in Table S1† show that, depending on their morphology, VO_2 nanomaterials with patches of a V_2O_5 surface layer exhibit better catalytic activity than pure V_2O_5 nanoparticles as well as V_2O_5 nanoparticles on different support surfaces.

The turnover number (TON) and turnover frequency (TOF) for the three different morphologies of VO_2 nanocatalysts are also compiled in Tables 1 and 2. For the oxidation of benzyl alcohol to benzaldehyde, the TON and TOF values range from 9.97 to 7.08 and from 2.49 to 1.77 h^{-1}, respectively. For the oxidation of furfuryl alcohol to furfural, the values are 8.00–3.94 and 2.00–0.99 h^{-1}, respectively. Urchin-like VO_2 nanoparticles had the highest, VO_2 nanorods the lowest TON and TOF values. The results are illustrated in Fig. 8 and 9. The reusability of the VO_2 nano-urchins, the best catalyst, was investigated in five cycles. The catalyst was essentially stable (activity decrease from 100% to ~96%, Fig. 9). The VO_2 materials are structurally stable as shown by the X-ray diffractogram (Fig. S4†) of the VO_x nanourchins measured after the catalytic application.

Based on the catalytic results obtained, we propose a possible reaction mechanism for the oxidation of alcohols over the VO_2 nanocatalysts (Fig. S5†). The adsorption of alcohols on the surface of nanocatalysts occur in the beginning of the catalytic cycle. Subsequently, breaking of O–H bond and loss of a proton may lead to the formation of VO_2-alkoxide on the

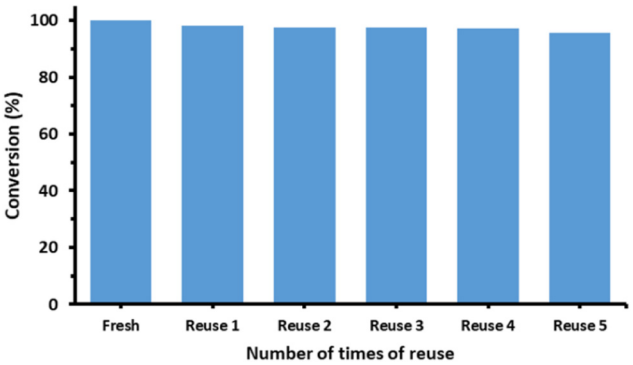

Fig. 9 Catalytic performance of VO_2 nano-urchins when reused.

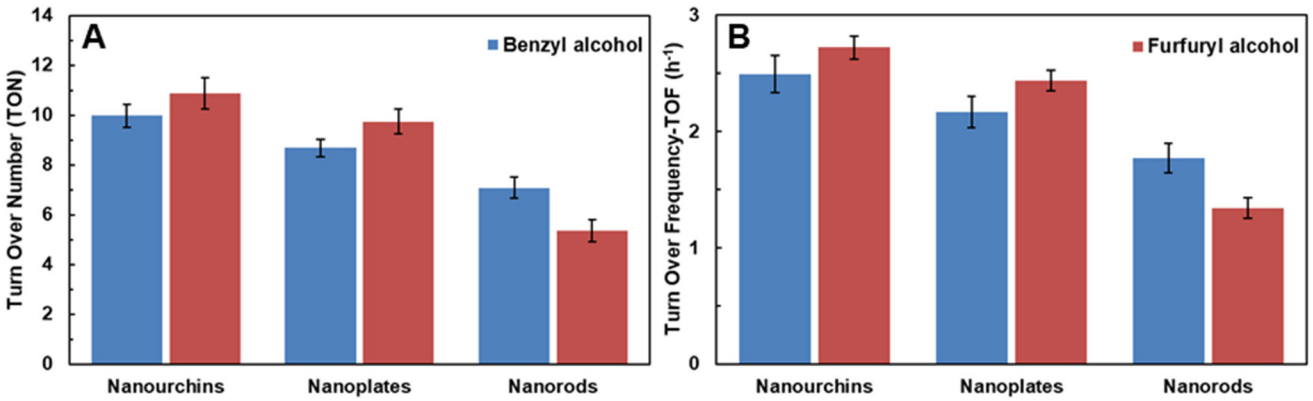

Fig. 8 TON and TOF values for as-synthesized VO_2 nanocrystals, (A) benzyl alcohol and (B) furfuryl alcohol.

surface of the cluster, which is suggested by the DFT simulations in an earlier study.[80] In the next step, the released proton is captured by adsorbed O_2 on the catalyst surface, which lead to the cleavage of the C–H bond of α-C. This may lead to the generation of desired carbonyl compound and regeneration of the VO_2 surface (IV).

Conclusion

By simple but very efficient reaction control, VO_2 nanocatalysts with different morphologies and activities could be prepared for the selective oxidation of alcohols to aldehydes. We demonstrated this by changing the composition of a binary solvent mixture, which established a facile new hydro-/solvothermal synthesis of VO_2 nanoparticles. VO_2 nanorods were obtained at water : ethanol ratios between 4 : 1 and 3 : 2. Polydisperse VO_2(B) nanorods were formed at a large water : ethanol ratio. At a water : ethanol ratio of 1 : 9 and in pure ethanol, aggregates of VO_x nanosheets were formed. The formation of these aggregates may be due to a lack of water leading to aggregation because of insufficient hydration of the products. The VO_2 phase identity was determined by TEM and X-ray diffraction on powder samples. XPS spectroscopy clearly showed the presence of V^{4+}, thus supporting the VO_2 phase assignment. Weak binding of alcohol surface ligands was demonstrated by IR and Raman spectroscopy. The catalytic activities of VO_2 particles in oxidation reactions were investigated using two model reactions, the oxidation of benzyl alcohol to benzaldehyde and the oxidation of furfuryl alcohol to furfural. All VO_2 particles were catalytically active. VO_2 particles with urchin-like morphology had the larger active BET surface area and showed the highest conversion for the oxidation of benzyl alcohol to benzaldehyde and furfuryl alcohol to furfural with 100% and 67% (spec. activities 3.01 and 2.41 mmol g^{-1} h^{-1}). VO_2 nanorods showed the lowest conversion with 71% and 33% (spec. activities 2.13 and 1.19 mmol g^{-1} h^{-1}). The conversion for alcohols in the presence of VO_2 particles with sheet-like morphology was slightly lower (87% and 60%) than for VO_2 with urchin-like morphology (spec. activities 2.61 and 2.16 mmol g^{-1} h^{-1}). The differences in catalytic activity can be attributed to the active surface area of the catalysts as a result of particle size. The VO_2 nanocatalysts are reusable; their activity remained stable even after several catalytic cycles. Our results show that (i) VO_2 is a good redox catalyst for the oxidation of alcohols, and (ii) mixed-valent vanadium oxides of the Magneli-type are not needed. (iii) The particle morphology has a strong effect on the catalytic activity of a solid, which for a given compound is (iv) determined to a large extent by the active surface area.

Experimental

Chemicals

All starting materials were used without further purification. Pluronic F-127, vanadyl acetylacetonate (98%, $VO(acac)_2$), and ethanol (p.a.), were purchased from Sigma Aldrich. Benzyl alcohol (BzOH, 99%), furfuryl alcohol (99%), 1-dodecanol (98%) and triethylamine were obtained from Acros Organics.

Synthesis of VO_2 (B) nanorods

In a typical synthesis, 150 mg of pluronic F-127 was dissolved in 5 mL of ethanol to which 140 mg of $VO(acac)_2$ was added. The resulting solution was stirred for 3 h. Subsequently, it was poured into 20 mL water in a 50 mL Teflon-lined autoclave and kept at 453 K (180 °C) for 24 h. The products were separated by centrifugation (15 min, 9000 rpm) and further purified by washing with 15 mL of ethanol. Finally, the nanoparticles were precipitated by centrifugation and dried in a vacuum oven at 313 K (40 °C) for 12 h. The product was stored at ambient temperature.

Synthesis of VO_2 sheets

To 150 mg of pluronic F127 dissolved in 24.7 mL of ethanol 140 mg of $VO(acac)_2$ was added, and the resulting solution was stirred for 4 h. Then, 0.3 mL of water was added, and this solution was transferred into a 50 mL Teflon-lined autoclave and kept at 453 K (180 °C) for 24 h. Finally, the products were washed, isolated and dried in a vacuum oven.

Synthesis of VO_2 urchins

140 mg of $VO(acac)_2$ were added to a 150 mg of pluronic F-127 solution in 25 mL of ethanol, and the solution was stirred for 4 h. Subsequently, the solution was transferred into a 50 mL Teflon-lined autoclave and heated to 453 K (180 °C) for 24 h. The products were washed, isolated and dried *in vacuo*.

Synthesis with dodecanol

Pluronic F127 (150 mg) was dispersed in 25 mL of dodecanol (25 mL) in a water bath at 313 K. 140 mg of $VO(acac)_2$ was added, and the solution was stirred for 4 h. Subsequently the reaction mixture was transferred into a 50 mL Teflon-lined autoclave and heated to 453 K for 24 h. The brown product was precipitated by centrifugation (9000 rpm, 10 min) and washed with 15 mL of ethanol.

Heat treatment of VO_2 urchins

The dried VO_2 was heated to 453 K in a corundum boat with a heating rate of 2 K min^{-1}. This temperature was kept for 4 h before the sample was allowed to cool down at a rate of 2 K min^{-1}.

Oxidation catalysis

The catalytic oxidations were performed using benzyl alcohol and furfuryl alcohol as substrates with VO_2 nanorods, -sheets and -urchin as catalysts. The reactions were performed in a 100 mL stainless steel autoclave reactor equipped with a mechanical stirrer. A typical procedure for the catalytic oxidation of alcohol was as follows. The autoclave reactor was charged with benzyl alcohol (0.61 mmol), trimethylamine (0.61 mmol), VO_2 nanorods (0.050 mmol), toluene (15 mL), and O_2 (14 bar) and the reaction solution was heated for 4 h at

150 °C. After completion of the reaction, the catalyst was separated by filtration. The recovered catalyst was washed with ethanol (25 mL), dried at 80 °C and reused. To determine the product selectivity, the liquid products were analyzed by gas chromatography (GC, 7890A) Agilent Technologies Inc., equipped with a flame ionization detector (FID) and a 19019S-001 HP-PONA column.

Characterization

Electron microscopy. All nanoparticles were characterized by transmission electron microscopy (TEM) using a Philips EM420 instrument with an acceleration voltage of 120 kV. Scanning electron microscopic analysis was carried out on a Zeiss LEO 906e. Sample were prepared by depositing dilute ethanolic suspensions of the nanoparticles on a carbon coated copper grid. High resolution (HR) TEM images, and energy dispersive X-ray (EDX) spectroscopy images were acquired on a FEI Tecnai F30 S-Twin microscope with a 300 kV field emission gun.

X-ray diffraction. X-ray diffraction patterns were recorded with a Bruker AXS D8 Discover diffractometer equipped with a HiStar detector using graphite monochromatized Cu Kα radiation. Samples were glued on top of glass using a VP/VA copolymer (vinylpyrrolidone/vinylacetate) solution in isopropanol. Crystalline phases were identified according to the PDF-2 database using the Bruker AXS EVA program suite.

X-ray photoelectron spectroscopy. The samples were measured with an ESCA from PREVAC equipped with an SCIENTA R4000 X-ray photoelectron spectrometer using Mg Kα radiation (330 W, 15 kV, 22 mA).

Infrared and Raman spectroscopy. FT-IR spectra were measured on a Bruker Tensor 27 spectrometer. The samples were prepared as KBr pellets. Raman spectra were recorded using a Horiba Jobin Yvon LabRAM HR 800 spectrometer equipped with a CCD-detector. The Raman spectrometer was coupled to an Olympus BX41 optical microscope applying 50× magnification with a slit width of 100 μm. A HeNe laser with a wavelength of 632.8 nm and a spot size of 2 × 2 μm was employed for excitation.

N_2 sorption experiments. Nitrogen sorption experiments were performed using a Quantachrome autosorb 6B instrument using N2 as the adsorbate at 77 K. The multipoint Brunauer–Emmett–Teller (BET) method was used to determine the specific surface area. All samples were dried in a vacuum oven for 12 h at 313 K before analysis.

Conflicts of interest

There are no conflicts to declare.

Author contributions

All authors have given approval to the final version of the manuscript.

Acknowledgements

The KSU authors extend their appreciation to the Deputyship for Research and Innovation, "Ministry of Education" in Saudi Arabia for funding this research (IFKSUOR3–103–4).

References

1 M. Liu, B. Su, Y. Tang, X. Jiang and A. Yu, *Adv. Energy Mater.*, 2017, **7**, 1700885.
2 J. Meyer, S. Hamwi, M. Kröger, W. Kowalsky, T. Riedl and A. Kahn, *Adv. Mater.*, 2012, **24**, 5408–5427.
3 H. Takagi and H. Y. Hwang, *Science*, 2010, **327**, 1601–1602.
4 C. Wu and Y. Xie, *Energy Environ. Sci.*, 2010, **3**, 1191–1206.
5 B. M. Weckhuysen and D. E. Keller, *Catal. Today*, 2003, **78**, 25–46.
6 C. Wu, F. Feng and Y. Xie, *Chem. Soc. Rev.*, 2013, **42**, 5157–5183.
7 J. Jeong, N. Aetukuri, T. Graf, T. D. Schladt, M. G. Samant and S. S. P. Parkin, *Science*, 2013, **339**, 1402–1405.
8 M. Brahlek, L. Zhang, J. Lapano, H.-T. Zhang, R. Engel-Herbert, N. Shukla, S. Datta, H. Paik and D. G. Schlom, *MRS Commun.*, 2017, **7**, 27–52.
9 G. Kieslich, G. Cerretti, I. Veremchuk, R. P. Hermann, M. Panthöfer, J. Grin and W. Tremel, *Phys. Status Solidi A*, 2016, **213**, 808–823.
10 M. Joos, G. Cerretti, I. Veremchuk, P. Hofmann, H. Frerichs, D. H. Anjum, T. Reich, I. Lieberwirth, M. Panthöfer, W. G. Zeier and W. Tremel, *Inorg. Chem.*, 2018, **57**, 1259–1268.
11 E. Strelcov, Y. Lilach and A. Kolmakov, *Nano Lett.*, 2009, **9**, 2322–2326.
12 Z. Khan, P. Singh, S. A. Ansari, S. R. Manippady, A. Jaiswal and M. Saxena, *Small*, 2021, **17**, 2006651.
13 S. Yang, Y. Gong, Z. Liu, L. Zhan, D. P. Hashim, L. Ma, R. Vajtai and P. M. Ajayan, *Nano Lett.*, 2013, **13**, 1596–1601.
14 **https://www.swatchgroup.com/en/swatch-group/innovation-powerhouse/industry-40/revolutionary-battery-belenos**. Accessed April 12 2023.
15 M. Yu, Y. Zang, H. Yan, X. Cheng, W. Zhao, C. Liang, Y. Tong, H. Tang and X. Lu, *Adv. Funct. Mater.*, 2015, **25**, 3534–3540.
16 I. E. Wachs, *Dalton Trans.*, 2013, **42**, 11762–11769.
17 F. Natalio, R. André, A. F. Hartog, B. Stoll, K. P. Jochum, R. Wever and W. Tremel, *Nat. Nanotechnol.*, 2012, **7**, 530–535.
18 K. Herget, F. Pfitzner, H. Frerichs, M. N. Tahir and W. Tremel, *Adv. Mater.*, 2018, **30**, e1707073.
19 *Handbook of Heterogeneous Catalysis*, ed. G. Ertl, H. Knözinger and J. Weitkamp, Wiley–VCH, Weinheim, 1997.
20 J. M. Thomas and W. J. Thomas, *Principles and Practice of Heterogeneous Catalysis*, VCH, Weinheim, 1997.
21 J. Hagen, *Industrial Catalysis, A Practical Approach*, 3rd edn, Wiley–VCH, Weinheim, 2015.

22 R. R. Langeslay, D. M. Kaphan, C. L. Marshall, P. C. Stair, A. P. Sattelberger and M. Delferro, *Chem. Rev.*, 2019, **119**, 2128–2191.
23 P. Mars and D. W. van Krevelen, *Chem. Eng. Sci.*, 1954, **3**, 41–59.
24 D. Matthey, J. G. Wang, S. Wendt, J. Matthiesen, R. Schaub, E. Lægsgaard, B. Hammer and F. Besenbacher, *Science*, 2007, **315**, 1692–1696.
25 J. H. Kwak, J. Hu, D. Mei, C.-W. Yi, D. H. Kim, C. H. F. Peden, L. F. Allard and J. Szanyi, *Science*, 2009, **325**, 1670–1673.
26 B. L. M. Hendriksen, M. D. Ackermann, R. van Rijn, D. Stoltz, I. Popa, O. Balmes, A. Resta, D. Wermeille, R. Felici, S. Ferrer and J. W. M. Frenken, *Nat. Chem.*, 2010, **2**, 730–734.
27 C. Wöll, *Phys. Chem. Chem. Phys.*, 2016, **18**, 19713–19721.
28 B. Frank, R. Fortrie, C. Hess, R. Schlögl and R. Schomaecker, *Appl. Catal., A*, 2009, **353**, 288–295.
29 K. Chen, N. Liu, M. Zhang and D. Wang, *Appl. Catal., B*, 2017, **212**, 32–40.
30 C. A. Carrero, R. Schloegl, I. E. Wachs and R. Schomaecker, *ACS Catal.*, 2014, **4**(10), 3357–3380.
31 M. C. Casey and D. E. Cliffel, *Anal. Chem.*, 2015, **87**, 334–337.
32 J. Haber, *Catal. Today*, 2009, **142**, 100–113.
33 R. Berenguer, M. O. Guerrero-Perez, I. Guzman, J. Rodríguez-Mirasol and T. Cordero, *ACS Omega*, 2017, **2**, 7739–7745.
34 K. An and G. A. Somorjai, *ChemCatChem*, 2012, **4**, 1512–1524.
35 D. Yun, Y. Song and J. E. Herrea, *ChemCatChem*, 2017, **9**, 3655–3669.
36 A. Chieregato, C. Bandinelli, P. Conception, D. Soriano, F. Puzzo, F. Basile, F. Cavani and J. M. Lopez-Nieto, *ChemSusChem*, 2017, **10**, 234–244.
37 A. Pan, H. B. Wu, L. Wu and X. W. Lou, *Angew. Chem.*, 2013, **125**, 2282–2286, (*Angew. Chem., Int. Ed.*, 2013, **52**, 2226–2230).
38 E. Uchaker, N. Zhou, Y. Li and G. Cao, *J. Phys. Chem. C*, 2013, **117**, 1621–1626.
39 N. Pinna, M. Willinger, K. Weiss, J. Urban and R. Schlögl, *Nano Lett.*, 2003, **3**(8), 1131–1134.
40 H. A. Therese, F. Rocker, A. Reiber, J. Li, M. Stepputat, G. Glasser, U. Kolb and W. Tremel, *Angew. Chem.*, 2005, **117**, 267–270, (*Angew. Chem., Int. Ed.*, 2005, **44**, 262–265).
41 Y. Liu, E. Uchaker, N. Zhou, J. Li, Q. Zhang and G. Cao, *J. Mater. Chem.*, 2012, **22**, 24439–24445.
42 N. Pinna and M. Niederberger, *Angew. Chem.*, 2008, **120**, 5372–5385, (*Angew. Chem. Int. Ed.*, 2008, **47**, 5292–5304).
43 R. Li and C.-Y. Liu, *Mater. Res. Bull.*, 2010, **45**, 688–692.
44 W. Li, S. Ji, Y. Li, A. Huang, H. Luo and P. Jin, *RSC Adv.*, 2014, **4**, 13026–13033.
45 K. Vikrant, S. Weon, K.-H. Kim and M. Sillanpää, *Photonics Nanostruct.*, 2022, **49**, 100993.
46 P. Liu, K. Zhu, Y. Gao, Q. Wu, J. Liu, J. Qiu, Q. Gu and H. Zheng, *CrystEngComm*, 2013, **15**, 2753–2760.
47 H. F. Xua, Y. Liu, N. Wei and S. W. Jin, *Optik*, 2014, **125**, 6078–6081.
48 K. K. Dey, D. Bhatnagar, A. K. Srivastava, M. Wan, S. Singh, R. R. Yadav and M. Deepa, VO_2 nanorods for efficient performance in thermal fluids and sensors, *Nanoscale*, 2015, **7**, 6159–6172.
49 L. Zhang, J. Yao, Y. Guo, F. Xia, F. Cui, B. Liu and Y. Gao, *Ceram. Int.*, 2018, **44**, 19301–19306.
50 Y. Zhang, M. Fan, X. Liu, G. Xie, H. Li and C. Huang, *Solid State Commun.*, 2007, **144**, 259–263.
51 P. Liu, Y. Xu, K. Zhu, K. Bian, J. Wang, X. Sun, G. Tai, Y. Gao, H. Luo, L. Lu and J. Liu, *J. Mater. Chem. A*, 2017, **5**, 8307–8316.
52 S. Zhong, Z. Zou, S. Le, C. Shu, S. Zhang and J. Geng, *ACS Appl. Nano Mater.*, 2022, **5**, 18023–18034.
53 S. Shi, Y. Yu, X. Feng, R. Qi and Y. Zhao, *Batteries*, 2023, **9**, 95.
54 A. Kojima, K. Okazaki, S. Ooi and K. Saito, *Inorg. Chem.*, 2009, **48**, 1168–1172.
55 O. Karahan, A. Tufani, S. Unal, I. B. Misirlioglu, Y. Z. Menceloglu and K. Serdur, *Nanomaterials*, 2021, **11**, 752.
56 S. Xiong, B. Xi, C. Wang, G. Zou, L. Fei, W. Wang and Y. Qian, *Chem. – Eur. J.*, 2007, **13**, 3076–3081.
57 D. M. Minic and V. A. Blagojevic, *CrystEngComm*, 2013, **15**, 6617–6624.
58 M. Niederberger and G. Garnweitner, *Chem. – Eur. J.*, 2006, **12**, 7282–7302.
59 H. Weingärtner and E. U. Franck, *Angew. Chem., Int. Ed.*, 2005, **44**, 2672–2692.
60 R. I. Walton, *Chem. – Eur. J.*, 2020, **26**, 9041–9069.
61 P. Scherrer, *Nachr. Ges. Wiss. Göttingen*, 1918, **26**, 98–100.
62 J. I. Langford and A. J. C. Wilson, *J. Appl. Crystallogr.*, 1978, **11**, 102–113.
63 J. T. Grant, C. A. Carrero, A. M. Love, R. Verel and I. Hermans, *ACS Catal.*, 2015, **5**, 5787–5793.
64 S. Barman, N. Maity, K. Bhatte, S. Ould-Chikh, O. Dachwald, C. Haeßner, Y. Saih, E. Abou-Hamad, I. Llorens, J.-L. Hazemann, K. Köhler, V. D′ Elia and J.-M. Basset, *ACS Catal.*, 2016, **6**, 5908–5921.
65 P. Shvets, O. Dikaya, K. Maksimova and A. Goikhman, *J. Raman Spectrosc.*, 2019, **50**, 1226–1244.
66 G. Silversmit, D. Depla, H. Poelman, G. B. Marin and R. De Gryse, *J. Electron Spectrosc. Relat. Phenom.*, 2004, **135**, 167–175.
67 S. H. Lee, H. M. Cheong, M. J. Seong, P. Liu, C. E. Tracy, A. Mascarenhas, J. R. Pitts and S. K. Deb, *J. Appl. Phys.*, 2002, **92**, 1893.
68 M. Pradhan, A. Roy, A. K. Sinha, R. Sahoo, D. Deb and T. Pal, *Dalton Trans.*, 2015, **44**, 1889–1899.
69 I. Mjejri, N. Etteyeb and F. Sediri, *Mater. Res. Bull.*, 2013, **48**, 3335–3341.
70 R. L. Frost, K. L. Erickson, M. L. Weier and O. Carmody, *Spectrochim. Acta, Part A*, 2005, **61**, 829–834.
71 U. Kolb, E. Mugnaioli and T. E. Gorelik, *Cryst. Res. Technol.*, 2011, **46**, 542–554.

72 E. Mugnaioli, I. Andrusenko, T. Schüler, N. Loges, R. E. Dinnebier, M. Panthöfer, W. Tremel and U. Kolb, *Angew. Chem., Int. Ed.*, 2012, **51**, 7041–7045.
73 M. A. Lange, Y. Krysiak, J. Hartmann, M. N. Tahir, M. Panthöfer, T. Reich, M. Mondeshki, U. Kolb and W. Tremel, *Adv. Funct. Mater.*, 2021, **30**, 1909051.
74 J. Mendialdua, R. Casanova and Y. Barbaux, *J. Electron Spectrosc. Relat. Phenom.*, 1995, **71**, 249–261.
75 A. Gloskovskii, S. A. Nepijko, G. Schönhense, H. A. Therese, A. Reiber, H. C. Kandpal, G. H. Fecher, C. Felser, W. Tremel and M. Klimenkov, *J. Appl. Phys.*, 2007, **101**, 084301.
76 A. Birkel, F. Reuter, D. Koll, S. Frank, R. Branscheid, M. Panthöfer, E. Rentschler and W. Tremel, *CrystEngComm*, 2011, **13**, 2487–2493.
77 Y. Xu, L. Zheng, C. Wu, F. Qi and Y. Xie, *Chem. – Eur. J.*, 2011, **17**, 384–391.
78 A. Pan, H. B. Wu, L. Yu, T. Zhu and X. W. Lou, *ACS Appl. Mater. Interfaces*, 2012, **4**, 3874–3879.
79 H. Pang, Y. Dong, S. L. Ting, J. Lu, C. Li, D.-H. Kim and P. Chen, *Nanoscale*, 2013, **5**, 7790–7794.
80 S. Zavahir, Q. Xiao, S. Sarina, J. Zhao, S. Bottle, M. Wellard, J. Jia, L. Jing, Y. Huang, J. P. Blinco, H. Wu and H.-Y. Zhu, *ACS Catal.*, 2016, **6**, 3580–3588.
81 K. Alagiri and K. R. Prabhu, *Tetrahedron*, 2011, **67**, 8544–8551.
82 G. K. Kara, J. Rahimi, M. Niksefat, R. Taheri-Ledari, M. Rabbani and A. Maleki, *Mater. Chem. Phys.*, 2020, **250**, 122991.
83 R. Upadhyay, S. Kumar and S. K. Maurya, *ChemCatChem*, 2021, **13**, 3594–3600.
84 N. Anbu, M. B. R. Kamalam, K. Sethuraman and A. Dhakshinamoorthy, *ChemistrySelect*, 2018, **3**, 12725–12733.
85 C. Srilakshmi, V. Basava, G. Ramesh and M. Manjunath, *ChemistrySelect*, 2020, **5**, 4500–4508.
86 J. Li, B. Ren, X. Yan, P. Li, S. Gao and R. Cao, *J. Catal.*, 2021, **395**, 227–235.